Formation of porous ice frameworks at room temperature

Yuan Liu[a,1,2], Weiduo Zhu[b,1], Jian Jiang[c], Chongqin Zhu[d], Chang Liu[e], Ben Slater[f], Lars Ojamäe[g], Joseph S. Francisco[d,2], and Xiao Cheng Zeng[c,2]

[a]School of Chemical Engineering and Technology, Sun Yat-sen University, Zhuhai 519082, China
[b]Department of Chemical Physics, University of Science and Technology of China, Hefei 230026, China
[c]Department of Chemistry, University of Nebraska-Lincoln, NE 68588, USA
[d]Department of Earth and Environmental Science and Department of Chemistry, University of Pennsylvania, Philadelphia, PA 19104, USA
[e]College of Physics, Liaoning University, Shenyang 110036, China
[f]Department of Chemistry, University College London, 20 Gordon Street, London W C1H 0AJ, UK
[g]Department of Physics, Chemistry and Biology, Linköping University, SE-581 83 Linköping, Sweden.
[1]Y.L and W.Z. contributed equally to this work.
[2]To whom correspondence maybe addressed. E-mail: liuy2265@mail.sysu.edu.cn (Y.L.); frjoseph@sas.upenn.edu (J.S.F.); xzeng1@unl.edu (X.C.Z.).
The authors declare no conflict of interest.

Bulk crystalline ices with ultralow densities have been demonstrated to be thermodynamically metastable at negative pressures. However, the direct formation of these bulk porous ices from liquid water at negative pressures is extremely challenging. Inspired by approaches toward porous media based on host–guest chemistry, such as metal–organic frameworks (MOFs) and covalent organic frameworks, we herein demonstrate via molecular dynamics simulations that a class of ultralow-density porous ices with upright channels can be formed spontaneously from liquid water at 300 K with the assistance of the carbon nanotube arrays. We refer to these porous ice polymorphs as water oxygen-vertex frameworks (WOFs). Notably, our simulations revealed that the liquid–WOF phase transition is first order and occurs at room temperature. All the WOFs exhibited the unique structural feature that they can be regarded as assemblies of nanoribbons of hexagonal bilayer ice (2D ice I) at their armchair or zigzag edges. Based on density functional theory calculations, a comprehensive phase diagram of the WOFs was constructed considering both the

thermodynamic and thermal stabilities of the porous ices at negative pressures. Like other types of porous media, these WOFs may be applicable to gas storage, purification, and separation. Moreover, these biocompatible porous ice networks may be exploited as medical-related carriers.

Significance

Crystalline ice with ultralow density is metastable at negative pressures, but is challenging to make via direct nucleation of liquid water at low temperature. Based on molecular dynamics simulations, here we show a class of ultralow-density porous ices which all exhibit water oxygen-vertex frameworks (WOFs), akin to the porous metal organic frameworks (MOFs). Notably, the WOFs can be formed spontaneously from liquid water at room temperature with the prearranged carbon nanotube array as the "guest array" and the structures of WOFs can be viewed as assemblies of nanoribbons of 2D hexagonal bilayer ice at the armchair edges. The lowest-density WOF presents exceptionally high gravimetric and volumetric hydrogen storage capacities (27.5 wt% and 111.7 g/L), even higher than that (70.85 g/L) of liquid H_2.

Ice is ubiquitous but mysterious, not any other substance possesses such a rich array of polymorphs from the best of our knowledge (1). Eighteen bulk polymorphs (or phases) of ice (ices I–XVIII) have been discovered over the past 100+ years. Except ice polymorphs exist at very high pressure, ice XVIII is recently revealed to exist at very high pressures of 100–400 GPa (2), while negative-pressure regions of the water phase diagram is attracting more and more attention. Recently, the structures of ices XVI and XVII were confirmed in the laboratory, whereas ice XVI is only stable at negative pressures between approximately −0.4 and −1 GPa (3), while ice XVII is a low-density porous ice containing spiral internal channels (4). Numerous zeolite-like porous ices have also recently been predicted to be metastable at negative pressures (5-11). Like many known porous materials, such as zeolites, metal–organic frameworks (MOFs) (12), and covalent organic frameworks (COFs) (13), porous ices may be applicable to gas storage, purification, and separation (14, 15), or even potentially possess medical applications owing to their lack of toxicity. However, in contrast to common ice (I_h), which is easily formed by the homogeneous ice nucleation of liquid water (16), it is extremely challenging to produce porous ices by the direct nucleation of liquid water at negative pressures (3). Recently, it suggested that the porous ice could be formed with the aid of suitable guests within liquid water (17, 18).

Motivated by host–guest chemistry, we herein demonstrate via molecular dynamics (MD) simulations that a class of ultralow-density porous ices (hosts) with upright channels can be formed spontaneously from liquid water at 300 K by using carbon nanotube (CNT) arrays as the guests. We refer to these porous ice polymorphs as water oxygen-vertex frameworks (WOFs), by analogy with MOFs and COFs. Extensive structural searches were performed over a wide range of CNT diameters from 0.2 to 1.4 nm while considering various spacings between the CNTs in the array. A series of hexagonal WOFs was observed from the structural searches in this work, and more WOFs could be achieved if the CNT array were arranged in other Brava lattice forms. For example, two distinct tetragonal WOFs were also obtained by using

the tetragonal arrangements of the CNT array in our simulations. Importantly, formation of these porous ices does not rely on the use of extreme negative-pressure conditions, in which the liquid–solid phase transitions would happen even at room temperature (300 K). Moreover, the hexagonal WOFs exhibited a unique structural feature in that they can be viewed as assemblies of nanoribbons of AA-stacked hexagonal bilayer ice (2D ice I (19, 20)) at their armchair edges or of AB-stacked bilayer ice. The thermodynamic and structural stabilities of these WOFs are further examined and the associated *P–T* phase diagram is constructed using a combination of density functional theory (DFT) calculations and MD simulations. Even when the CNTs are removed, the guest-free porous WOFs are found to remain stable, which would be a new type of promising hydrogen storage materials.

Results and discussion

Formation of various WOFs using CNT arrays as guest. As shown in Fig. 1A and *SI Appendix*, Fig. S1, zigzag CNTs with a length of 8 nm were arranged in the form of a hexagonal array with tunable spacing between the CNTs, while the diameters of the CNTs ranged between 0.2 and 1.4 nm as listed in *SI Appendix*, Table S1. As shown in Figs. 1B and 1C, ten different WOFs were obtained during the structural search based on independent MD simulations at a constant temperature of 300 K. The porous ice structures achieved using different CNT parameters were denoted WOF I_a, I_b, I_c, II_a, II_b, and II_c, according to a labeling scheme based on the structural characteristics as described in the following subsection. The range of the CNT-array parameters for each WOF occurrence is plotted in Figs. 1B and 1C, and the structures are depicted in Fig. 1D and *SI Appendix*, Fig. S2. The water freezing processes are presented in *SI Appendix*, Movies S1–S6.

As listed in *SI Appendix*, Table S2 and plotted in *SI Appendix*, Fig. S3, the inter-CNT average spacing and the CNT diameter follow linear relations for all the type-I, type-II, and mixed porous ice phases. Based on the fitted functions in *SI Appendix*, Fig. S3, the inter-CNT spacing parameters for more WOFs could be found

by using CNTs with larger diameters, which would accelerate the predictions of WOFs and reduce the computation cost. In addition to the 4-site TIP4P/ice water potential, the WOFs can be spontaneously formed at room temperature by using the 3-site SPC/E water potential, as shown in *SI Appendix*, Figs. S4*A* and S4*B*.

As shown in Figs. 2A–2C, the potential energies of each system clearly decreased with increasing simulation time. The freezing transition was typically observed in approximately 20 ns, as seen from the decreasing trend of potential energies. Moreover, first-order phase transitions were observed in the MD simulations during both the heating and cooling processes, as indicated by the sharp changes in the potential energy and hysteresis of the potential energies shown in Figs. 2D–2I. The freezing temperature can be estimated from the abrupt energy drop during the cooling process. More interestingly, the estimated freezing temperatures of these porous ice networks, which were 305 K for WOF I_a, 310 K for WOF I_b, 300 K for WOF I_c, 320 K for WOF II_a, 310 K for WOF II_b, and 300 K for WOF II_c, were all higher than the transition temperature of bulk ice I_h. Notably, the estimated freezing temperature would vary slightly by using different CNT parameters for the same WOF structure, as shown in *SI Appendix*, Figs S5A and S5B.

Structures, stabilities, and *P–T* phase diagram of the WOFs. The unit-cell structures of the hexagonal WOFs obtained during the spontaneous freezing processes in the MD simulations are presented in Fig. 3 and *SI Appendix*, Figs. S6 and S7. As shown in Fig. 3, the nodes of these WOFs consisted of three edge-shared pentagons, while the linkers were nanoribbons of AA-stacked hexagonal bilayer ice (2D ice I (19, 20)). Consequently, these hexagonal WOFs can be regarded as assemblies of nanoribbons of hexagonal bilayer ice connected through their armchair edges. As mentioned above, we refer to these frameworks as type-I WOFs. The length of the linker was zero for the structure of WOF I_a and then gradually increased from WOF I_b to I_f, as illustrated by the successively increasing number of four-membered rings in the top views of Fig. 3. Meanwhile, the polygonal cross section of the WOF channels became larger and larger, from 12-membered rings in I_a to 18-membered

rings in I_b, 24-membered rings in I_c, 30-membered rings in I_d, 36-membered rings in I_e, and 42-membered rings in I_f.

As shown in *SI Appendix*, Fig. S7, the nodes of the type-II WOFs were a hexagon, while the linkers were nanoribbons of AB-stacked bilayer ice (21) of various width. The linker width gradually increased from II_a to II_e, as demonstrated by the gradually increasing number of four-membered rings in the top views. The polygonal cross section of the channels of the type-II WOFs also gradually increased from 12-membered rings to 36-membered rings. As depicted in *SI Appendix*, Fig. S8, the structures of the type-III WOFs were composed of nodes of hexagons, with nanoribbons of AA-stacked hexagonal bilayer ice as the linkers. The nodes and linkers were connected at the zigzag edges of the AA-stacked bilayer ice.

The structural, energetic, and mechanical properties of the WOFs are listed in Table 1. Compared with the corresponding experimental values for ice XI, the computed volume and lattice energy of ice XI were overestimated by 2.7% and 6.7%, respectively (22-24). For WOFs of the same type, those with higher mass density tended to possess a lower lattice energy and therefore greater stability at 0 K. The porosity of a WOF is proportional to the diameter of the WOF channel but inversely proportional to the mass density. Therefore, the lattice energies of the WOFs decreased with increasing porosity, as shown in Fig. 4A. Notably, except for II_a, the lattice energies of the type-I WOFs were slightly higher than those of the type-II and type-III WOFs at the same porosity, suggesting that the structures of the type-I and II_a WOFs are likely the intrinsic structures.

On the basis of the Birch–Murnaghan equation of state (25), the E versus V curves (lattice energy versus volume per water molecule) were plotted in Fig. 4B. The equation of state for each WOF was consistent with the relation between the lattice energy and mass density. The relative enthalpies at 0 K of the type-I WOFs and II_a with respect to ice XI were further computed, as shown in Fig. 4C. The solid–solid phase transition pressure at 0 K can be inferred from this plot. At 0 K, ice XI would transform to the WOF I_f at −1700 bar without considering the zero-point vibrational

energies; this pressure is less negative than those for the transitions between ice XI and the other WOFs considered in this study.

The dynamic stabilities of three WOF structures, namely, 0_a, I_a, and II_a, were examined using DFT/vdW-DF2 (26) calculations. The computed phonon dispersion spectra are presented in *SI Appendix*, Figs. S9–S11. Only small negative frequencies for the acoustic modes were observed, especially for WOF II_a (*SI Appendix*, Fig. S11), due to the inaccurate handling of the translational invariance originated from the discreteness of the fast Fourier transform grids. Hence, the bare WOFs, particularly II_a, are expected to be dynamically stable.

The thermal stabilities of WOFs I_a, I_b, and I_c were evaluated at pressures of −1000, 1, and 100 bar, respectively, via MD simulations (as shown in Fig. 4D) with incremental increasing temperature. As the temperature was increased in steps of 10 K, the WOF structures eventually broke at the highest temperatures examined. At 100 bar, the solid structures remained intact until 280 K for I_a, 260 K for I_b, and 190 K for I_c, as indicated by the sharp increase in mass density to approximately 1.0 g/cm^3 at 290 K for I_a, 270 K for I_b, and 200 K for I_c. At 1 bar, the highest temperatures at which each WOF remained intact for 50 ns were 280, 260, and 210 K for I_a, I_b, and I_c, respectively. In contrast, at −1000 bar, the structure of I_a remained intact for 50 ns at temperatures of up to 290 K, exceeding those at 1 and 100 bar. The I_b and I_c structures remained intact until 280 and 260 K, respectively, which were also higher than those at 1 and 100 bar. In particular, for the lower-density WOF I_c, the estimated temperature corresponding to the thermal stability limit (260 K) at −1000 bar was considerably higher than the values of 210 K (at 1 bar) and 190 K (at 100 bar). Notably, at −1000 bar, the mass densities of both I_b and I_c decreased abruptly when the temperature was increased beyond the corresponding stability limit owing to the sudden structural expansion at negative pressure, as shown in *SI Appendix*, Fig. S12. In general, the temperature corresponding to the thermal stability limit was higher at lower pressure, and structures with higher density remained intact at higher temperatures.

Fig. 4E depicts the *P–T* phase diagram constructed on the basis of Gibbs free-energy computations, for which the vibrational thermal energy corrections and entropies were obtained from normal-mode analysis (6, 27). In *SI Appendix*, Fig. S13, the relative Gibbs free energy versus pressure at various temperatures (in 25 K intervals) was plotted. Among the WOFs considered, the phase boundary bordering ice I_h (as indicated by the blue line in Fig. 4E) appears always to be the WOF I_f, suggesting that the phase transition between ice I_h and I_f would occur prior to those between ice I_h and the other WOFs. In addition, we constructed a *P–T* phase diagram based on the Gibbs free energies computed using the Einstein molecule method (5, 7, 28, 29) and the TIP4P/2005 water potential. As depicted in *SI Appendix*, Fig. S14, qualitatively the same results were obtained as those shown in Fig. 4E (based on the TIP4P/ice water potential), i.e., only I_f appeared to be immediately adjacent to the ice I_h phase on the *P–T* phase diagram.

It should be noted that the *P–T* phase diagram (Fig. 4E) was constructed on the basis of the computed Gibbs free energies, however, the structure maybe unstable at more negative pressures even if the Gibbs free energy is lower. A more reasonable approach to constructing the *P–T* phase diagram is to consider both the Gibbs free energies and the thermal stability limit for each polymorph, as previously described by Matsui *et al*.(10) As shown in *SI Appendix*, Fig. S13, for example, the Gibbs free energy of I_f was the lowest for pressures below −1609 bar at 25 K, indicating that I_f is the thermodynamically metastable structure under these *P–T* conditions. However, the structure of I_f can only remain stable until −3800 bar at 25 K owing to the structure stability limit (−3800 bar) revealed by the MD simulations. Next, the Gibbs free energy of I_e was the second lowest at 25 K and pressures below −1609 bar, which became the lowest value for pressures beyond the structure stability limit of I_f (−3800 bar). According to the MD simulations, the structure stability limit of the I_e structure is −4200 bar at 25 K. Consequently, at pressures below −4200 bar, I_d becomes the most stable structure. Eventually, the pressure regions were identified for all the WOFs at 25 K. As such, the pressure regions for each WOF were

also identified at other temperatures. Thus, the more complete *P–T* phase diagram presented in Fig. 4F was constructed by combining the results of the Gibbs free energy versus pressure plots with the structure stability limits for each WOF at various temperatures. As shown in Fig. 4F, the negative-pressure region below the stability region for ice I_h in the *P-T* phase diagram is split into multiple strips, where each strip corresponds to a stable WOF.

Besides hexagonal WOFs, other classes of WOFs can also be generated by using CNT array pre-arranged in other Brava lattice forms. For example, two distinct structures of tetragonal WOFs are spontaneously formed in our MD simulations with the CNTs pre-arranged in tetragonal arrays as shown in *SI Appendix*, Fig. S15. As such, we anticipate that the *P–T* phase diagram in the negative-pressure region would be sliced into denser strips as more WOFs are identified.

Hydrogen and methane storage by using WOF. To relieve society's reliance on fossil fuels, green hydrogen was widely viewed as a sustainable fuel while methane was considered as the transitional fuel (30, 31). The U.S. Department of Energy (DOE) established targets for the onboard methane and hydrogen storage media to enable widespread commercialization of electric fuel-cell vehicles, which are 0.5 g/g for the gravimetric storage capacity of CH_4 and 263 cm^3 (at standard temperature and pressure, STP)/cm^3 for the volumetric storage capacity of CH_4; and 5.5 wt% for the gravimetric storage capacity of H_2 and 40 g/L for the volumetric storage capacity of H_2 in the year of 2025 (31, 32). However, most hydrogen and methane storages today still exhibit insufficient gravimetric and volumetric capacity, a bottleneck to impede the wide use of hydrogen and methane as alternative fuels for auto transportation. Currently, high pressures (*e.g.* 700 bar for H_2 and 250 bar for CH_4) are needed for the fuel cell electric vehicle models in service around the world even though such high pressures are unsafe and costly (31, 32). Hence, materials with sufficiently high gravimetric and volumetric capacities are demanded for the safe and low-cost H_2 and CH_4 storage.

The highly porous WOF structures presented in this work could be a promising

medium for gas storage. As depicted in Fig. 5A and 5B, for example, a relatively large amount of hydrogen and methane molecules can be filled into the channels of WOF I_f. For H_2 encapsulated in I_f, the computed adsorption energy per hydrogen molecule is about –5.0 kJ/mol based on the vdW-DF2 functional (see *SI Appendix*, Table S3), close to the heat of hydrogen adsorption (Q_{st} = 4 kJ/mol) in the benchmark MOF of NU-1501-Al at low loading. This adsorption energy value is also close to the enthalpy of hydrogen adsorption (4.9 kJ/mol) computed from grand canonical Monte Carlo simulation at low pressure (32). The adsorption energy of CH_4 in I_f is about three times higher than that of H_2.

To promote the use of gas storage at low pressures, we evaluated thermal stabilities of hydrogen and methane encapsulated in WOF I_f at 100 bar and 5 bar, respectively. As depicted in Fig. 5C and 5D, H_2 and CH_4 containing I_f remains stable at 100 bar and 77 K. At 5 bar, the crystalline structure of I_f with H_2 enclosed would break at 110 K (see *SI Appendix*, Fig. S16A), while the crystalline structure of I_f with CH_4 enclosed would break at 180 K (see *SI Appendix*, Fig. S16B). Notably, both the gravimetric and volumetric storage capacity of H_2 (27.5 wt% and 111.7 g/L) in I_f are much higher than those in NU-1501-Al (14.5 wt% and 47.9 g/L) (32) at 100 bar and 77 K, as shown in Fig. 5E. Meanwhile, the volumetric density of H_2 in I_f at 100 bar and 77 K is also much higher than that (70.85 g/L) (33) of liquid H_2 at 1 bar and 20 K, suggesting that the relative hydrogen storage capacity of I_f is more superior than hydrogen liquidation. As shown in Fig. 5F, the gravimetric storage capacity of CH_4 (0.55 g/g at 100 bar and 77 K) in I_f is lower than that (0.66 g/g at 100 bar and 270 K) (32) in the MOF of NU-1501-Al. However, the volumetric storage capacity of CH_4 (529.4 cm^3 (STP)/cm^3 at 100 bar and 77 K) in I_f is higher than that (262 cm^3 (STP)/cm^3 at 100 bar and 270 K) in NU-1501-Al (32).

Conclusion

In this work, we observed spontaneous first-order freezing transition from liquid water to the WOFs in MD simulations at 300 K with hexagonal CNT array being used

as the guest. Hexagonal WOF polymorphs were obtained by using the CNTs with various diameters and appropriate int-CNT spacings. More WOFs could be achieved with the CNTs being pre-arranged in different Brava lattice, as suggested by the formation of two distinct WOFs with pre-arranged tetragonal CNT arrays. The WOFs exhibited unique structural features in that they can be viewed as assemblies of nanoribbons of AA-stacked hexagonal bilayer ice at their armchair/zigzag edges or of AB-stacked bilayer ice. DFT calculations showed that the type-I and II_a WOFs were more stable than the other types, and the lattice energies of the WOFs decreased with increasing porosity. The *P–T* phase diagram of the WOFs at negative pressures was constructed based on Gibbs free-energy computation and the determined thermal stability limits. Each WOF polymorph occupied a strip-like area in the negative-pressure region of the *P–T* phase diagram below the ice I_h phase. Finally, the WOFs were suggested to be promising hydrogen storage media with exceptionally high gravimetric and volumetric storage capacities (27.5 wt% and 111.7 g/L), much higher than those of liquid H_2, to meet the DOE target for the alternative and renewable fuels for electric vehicles.

Methods

As presented in *SI Appendix*, Fig. S1, CNTs with a length of 8 nm were arranged in a hexagonal array. Water layers with a thickness of 2 nm were situated both above the top ends and below the bottom ends of the CNTs. Periodic boundary conditions were used in the *x* and *y* directions, while a 24 nm vacuum slab was added in the *z* direction. The MD simulations were conducted in the constant temperature and volume (*NVT*) ensemble. The carbon atoms of the CNTs were frozen in the GROMACS program (34). The system temperature was controlled at 300 K using the Nosé–Hoover thermostat (note that the melting point of the employed water potential (TIP4P/Ice) was 272 K) (35). The Lennard-Jones (LJ) parameters of the carbon atoms were taken from the OPLS potential model included in the GROMACS program. The cross LJ interaction parameters between water and the carbon atoms were given by the

Lorentz–Berthelot rule. In the MD simulations, Newton's equations of motion were integrated with a time step of 1 fs using the leap-frog algorithm. If the solid structure did not occur after 30 ns, a new simulation was performed after modifying the inter-CNT distance ***D***. For the thermal stability evaluations, MD simulations in the *NPT* ensemble were conducted at the stated pressures and temperatures. If the structure remained intact, as indicated by little change in the mass density, new simulations were performed after modifying the pressure and temperature until the solid structure broke. For the stability evaluations of I_a, I_b, and I_c shown in Fig. 4*D* and the stability of I_f occupied by H_2/CH_4, simulation time of 50 ns was carried out for each simulation. For the search of thermal stability limit of each structure to construct the phase diagram shown in Fig. 4F, simulation time of 20 ns was undertaken for each simulation due to the expensive computation cost.

For the structural relaxation of each WOF, DFT calculations were performed by adopting the nonlocal-dispersion corrected functional vdW-DF2 (26) and the PAW potentials implemented in the VASP 5.4 software package (36, 37). The energy cutoff for the plane-wave was taken as 800 eV, and the *k*-point grids were sampled with a uniform spacing of $2\pi \times 0.04$ Å^{-1}. The phonon spectra were calculated using the density functional perturbation theory (DFPT) method implemented in the Phonopy program associated with the VASP software package (38), for which the cutoff energy was set to 700 eV, and the *k*-point grids were sampled with a uniform spacing of $2\pi \times 0.05$ Å^{-1}. For the hydrogen storage in WOF I_f, 90 – 300 H_2 molecules were separately encapsulated in the unit cell of I_f with 88 H_2O, and for the methane storage in WOF I_f, 120 CH_4 molecules were encapsulated in the unit cell of I_f. To this end, the nonlocal-dispersion corrected functional vdW-DF2 and the PAW potentials were also employed in the VASP software package. The cutoff energy was set to 700 eV and the Brillouin zone was sampled by Gamma point for the gas molecules occupied structures.

To compute the vibrational thermal energies, normal-mode analyses were used in conjunction with the CVFF (39) force field. As shown in *SI Appendix*, Fig. S17, the

frequencies calculated using the normal-mode analysis were similar to those obtained from the phonon-spectrum calculations based on the vdW-DF2 functional. Moreover, the *P–T* phase diagram constructed on the basis of the Gibbs free energy computations (including corrections for the vibrational thermal energy and entropy) (6, 27) was consistent with that constructed from the Gibbs free energy computations using the Einstein molecule method.[28]

References

1. C. G. Salzmann, P. G. Radaelli, B. Slater, J. L. Finney, The polymorphism of ice: five unresolved questions. *Phys. Chem. Chem. Phys.* **13**, 18468 (2011).
2. M. Millot*, et al.*, Nanosecond X-ray diffraction of shock-compressed superionic water ice. *Nature* **569**, 251-255 (2019).
3. A. Falenty, T. C. Hansen, W. F. Kuhs, Formation and properties of ice XVI obtained by emptying a type sII clathrate hydrate. *Nature* **516**, 231 (2014).
4. L. Rosso, M. Celli, L. Ulivi, New porous water ice metastable at atmospheric pressure obtained by emptying a hydrogen-filled ice. *Nat. Commun.* **7**, 13394 (2016).
5. Y. Liu*, et al.*, An ultralow-density porous ice with the largest internal cavity identified in the water phase diagram. *Proc. Natl. Acad. Sci. USA* **116**, 12684 (2019).
6. Y. Liu and L. Ojamäe, Clathrate ice sL: a new crystalline phase of ice with ultralow density predicted by first-principles phase diagram computations. *Phys. Chem. Chem. Phys.* **20**, 8333-8340 (2018).
7. Y. Y. Huang*, et al.*, A new phase diagram of water under negative pressure: The rise of the lowest-density clathrate s-III. *Sci. Adv.* **2**, e1501010 (2016).
8. Y. Y. Huang, C. Q. Zhu, L. Wang, J. J. Zhao, X. C. Zeng, Prediction of a new ice clathrate with record low density: A potential candidate as ice XIX in guest-free form. *Chem. Phys. Lett.* **671**, 186-191 (2017).
9. T. Matsui, M. Hirata, T. Yagasaki, M. Matsumoto, H. Tanaka, Communication: Hypothetical ultralow-density ice polymorphs. *J. Chem. Phys.* **147**, 091101 (2017).
10. T. Matsui, T. Yagasaki, M. Matsumoto, H. Tanaka, Phase diagram of ice polymorphs under negative pressure considering the limits of mechanical stability. *J. Chem. Phys.* **150**, 041102 (2019).
11. E. A. Engel, A. Anelli, M. Ceriotti, C. J. Pickard, R. J. Needs, Mapping uncharted territory in ice from zeolite networks to ice structures. *Nat. Commun.* **9**, 2173 (2018).
12. H. Li, M. Eddaoudi, M. O'Keeffe, O. M. Yaghi, Design and synthesis of an exceptionally stable and highly porous metal-organic framework. *Nature* **402**, 276 (1999).
13. A. P. Cote*, et al.*, Porous, crystalline, covalent organic frameworks. *Science* **310**, 1166 (2005).
14. D. Banerjee*, et al.*, Metal-organic framework with optimally selective xenon adsorption and separation. *Nat. Commun.* **7**, 11831 (2016).
15. J. T. A. Jones*, et al.*, Modular and predictable assembly of porous organic molecular crystals. *Nature* **474**, 367 (2011).
16. L. Lupi*, et al.*, Role of stacking disorder in ice nucleation. *Nature* **551**, 218 (2017).
17. A. Kumar, A. H. Nguyen, R. Okumu, T. D. Shepherd, V. Molinero, Could Mesophases Play a

Role in the Nucleation and Polymorph Selection of Zeolites? *J. Am. Chem. Soc.* **140**, 16071 (2018).

18. T. Yagasaki, M. Yamasaki, M. Matsumoto, H. Tanaka, Formation of hot ice caused by carbon nanobrushes. *J. Chem. Phys.* **151**, 064702 (2019).
19. K. Koga, X. C. Zeng, H. Tanaka, Freezing of confined water: A bilayer ice phase in hydrophobic nanopores. *Phys. Rev. Lett.* **79**, 5262-5265 (1997).
20. R. Z. Ma*, et al.*, Atomic imaging of the edge structure and growth of a two-dimensional hexagonal ice. *Nature* **577**, 60 (2020).
21. W. D. Zhu*, et al.*, Water confined in nanocapillaries: two-dimensional bilayer squarelike ice and associated solid-liquid-solid transition. *J. Phys. Chem. C* **122**, 6704 (2018).
22. A. J. Leadbetter*, et al.*, The equilibrium low-temperature structure of ice. *J. Chem. Phys.* **82**, 424-428 (1985).
23. E. Whalley, Energies of the phases of ice at zero temperature and pressure. *J. Chem. Phys.* **81**, 4087-4092 (1984).
24. Y. Liu and L. Ojamäe, Raman and IR Spectra of Ice Ih and Ice XI with an Assessment of DFT Methods. *J. Phys. Chem. B* **120**, 11043-11051 (2016).
25. F. Birch, Finite elastic strain of cubic crystals. *Phys. Rev.* **71**, 809-824 (1947).
26. K. Lee, E. D. Murray, L. Z. Kong, B. I. Lundqvist, D. C. Langreth, Higher-accuracy van der Waals density functional. *Phys. Rev. B* **82**, 081101R (2010).
27. A. Lenz and L. Ojamäe, Structures of the I-, II- and H-Methane Clathrates and the Ice-Methane Clathrate Phase Transition from Quantum-Chemical Modeling with Force-Field Thermal Corrections. *J. Phys. Chem. A* **115**, 6169-6176 (2011).
28. C. Vega and E. G. Noya, Revisiting the Frenkel-Ladd method to compute the free energy of solids: The Einstein molecule approach. *J. Chem. Phys.* **127**, 154113 (2007).
29. M. M. Conde, C. Vega, G. A. Tribello, B. Slater, The phase diagram of water at negative pressures: Virtual ices. *J. Chem. Phys.* **131**, 034510 (2009).
30. A. Schoedel, Z. Ji, O. M. Yaghi, The role of metal-organic frameworks in a carbon-neutral energy cycle. *Nature Energy* **1**, 1-13 (2016).
31. M. D. Allendorf*, et al.*, An assessment of strategies for the development of solid-state adsorbents for vehicular hydrogen storage. *Energy Environ. Sci.* **11**, 2784-2812 (2018).
32. Z. J. Chen*, et al.*, Balancing volumetric and gravimetric uptake in highly porous materials for clean energy. *Science* **368**, 297-303 (2020).
33. J. W. Leachman, R. T. Jacobsen, S. G. Penoncello, E. W. Lemmon, Fundamental Equations of State for Parahydrogen, Normal Hydrogen, and Orthohydrogen. *J. Phys. Chem. Ref. Data* **38**, 721 (2009).
34. D. Van der Spoel*, et al.*, GROMACS: Fast, flexible, and free. *J. Comput. Chem.* **26**, 1701-1718 (2005).
35. J. L. F. Abascal, E. Sanz, R. G. Fernandez, C. Vega, A potential model for the study of ices and amorphous water: TIP4P/Ice. *J. Chem. Phys.* **122**, 234511 (2005).
36. G. Kresse and J. Furthmuller, Efficient iterative schemes for ab initio total-energy calculations using a plane-wave basis set. *Phys. Rev. B* **54**, 11169-11186 (1996).
37. G. Kresse and D. Joubert, From ultrasoft pseudopotentials to the projector augmented-wave method. *Phys. Rev. B* **59**, 1758-1775 (1999).
38. S. Baroni, S. de Gironcoli, A. Dal Corso, P. Giannozzi, Phonons and related crystal properties

from density-functional perturbation theory. *Rev. Mod. Phys.* **73**, 515-562 (2001).

39. C. L. Lawson*, et al.*, Flexibility of the DNA-binding domains of trp repressor. *Proteins: Struct., Funct., Genet.* **3**, 18-31 (1988).

ACKNOWLEDGEMENTS. Y.L. and C.L. were supported by the National Natural Science Foundation of China (No. 21703006 and 11772144), Y.L. also supported by the Fundamental Research Funds for the Central Universities, Sun Yat-sen University, 2021qntd13, and L.O. was supported by the Swedish Research Council (VR). Computer resources were supplied by the Swedish National Supercomputer Centre (NSC) via the Swedish National Infrastructure for Computing (SNIC). J.S.F. and X.C.Z. acknowledged computational support by the University of Nebraska Holland Computing Center.

Author contributions: Y.L., J.S.F., and X.C.Z. designed the research; Y.L., W.Z., and X.C.Z. performed the research; Y.L., J.S.F., and X.C.Z. contributed new reagents/analytical tools; Y.L., W.Z., J.J., C.Z., C.L., B.S., L.O., J.S.F., and X.C.Z. analyzed the data; and Y.L., W.Z., L.O., J.S.F., and X.C.Z. wrote the paper.

Table 1. Structural, energetic, and mechanical properties of ice XI (as reference) and type-I, type-II, and type-III hexagonal WOFs.

Phase	N	ρ (g/cm^3)	V_{cell} (Å^3)	$D_{channel}$ (Å)	n-polygonal channel	Porosity	E_{latt} (kJ/mol)	B_0 (GPa)
Ice XI	8	0.91 (0.93*)	264 (257*)	—	—	0	−63.05 (−59.07†)	12.46
0_a	6	0.63	283	8.58	12	0.30	−54.08	7.11
I_a′	32	0.72	1322	10.01	12	0.20	−59.92	—
I_a	28	0.76	1105	10.20	12	0.16	−60.04	8.87
I_b	40	0.59	2014	14.89	18	0.34	−58.68	6.80
I_c	52	0.49	3172	19.31	24	0.46	−57.56	5.08
I_d	64	0.42	4571	23.94	30	0.54	−56.77	3.99
I_e	76	0.36	6277	28.41	36	0.60	−56.69	3.36
I_f	88	0.32	8152	32.82	42	0.64	−56.12	2.83
II_a	24	0.72	993	10.23	12	0.20	−59.59	9.24
II_b	36	0.58	1867	15.32	18	0.36	−57.14	6.65
II_c	48	0.48	3002	19.74	24	0.47	−56.28	5.08
II_d	60	0.41	4397	24.56	30	0.55	−55.63	3.88
II_e	72	0.36	6067	29.38	36	0.61	−55.17	3.46
III_a	24	0.52	1376	15.76	24	0.42	−56.36	—
III_b	36	0.40	2673	23.05	30	0.56	−55.96	—
III_c	48	0.33	4410	30.95	36	0.64	−55.60	—

Notes: N (number of water molecules per unit cell), ρ (mass density), V_{cell} (volume of each unit cell), $D_{channel}$ (diameter of the channel in the WOF structure), n-polygonal channel (number of edges on the intersecting surface of the channel), porosity = $(V_{cell} - N \times V_{H2O})/V_{cell}$, where V_{H2O} is the volume per water molecule for ice XI, E_{latt} (lattice energy per water molecule, DFT computation using the vdW-DF2 functional), B_0 (bulk modulus). *Ref. 23, †Ref. 24 and 25.

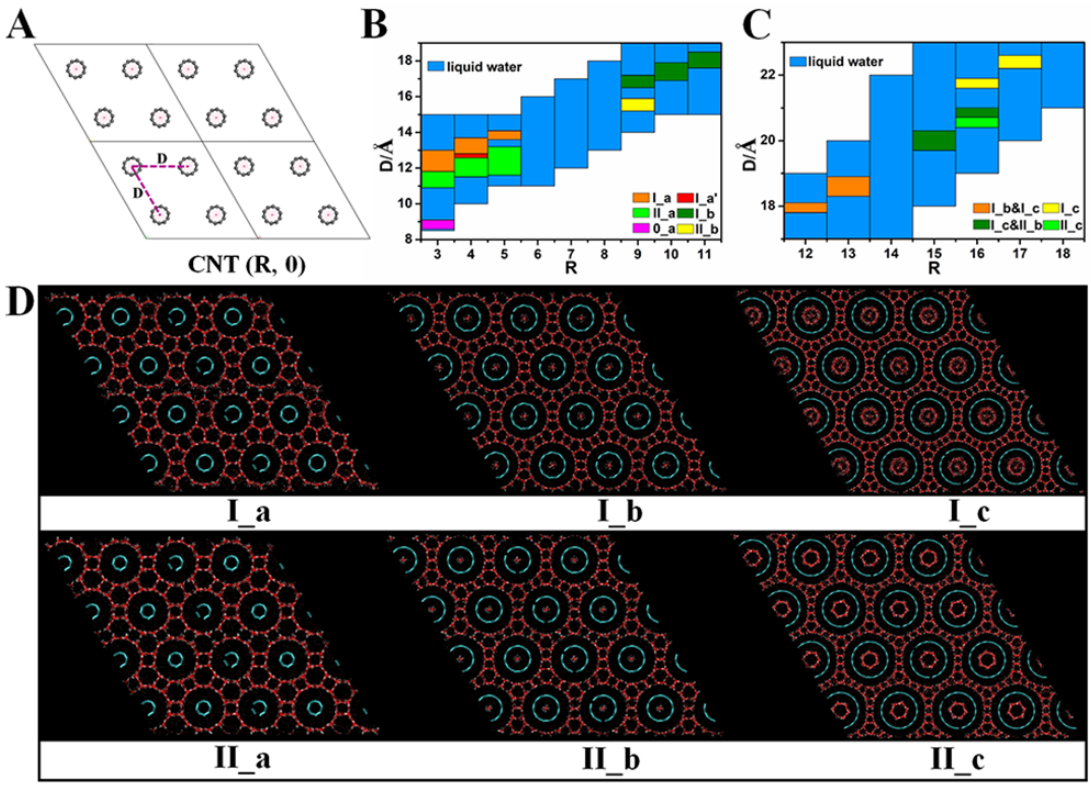

Fig. 1. WOFs formed at 300 K by using CNT arrays as the guests. (A) The CNTs (**R**, 0) were arranged in a hexagonal array with inter-CNT spacing ***D***. The CNT array was fixed in the liquid water (for clarity, the liquid water is not shown). (B) Structural search of the WOFs with various diameters of CNT (**R**, **0**) (**R**=3–11) and inter-CNT spacings ***D***. (C) Structural search of the WOFs with various diameters of CNTs (**R**, **0**) (**R**=12–18) and inter-CNT spacings ***D***. (D) Six distinct hexagonal WOFs spontaneously formed in the MD simulations at a constant temperature of 300 K. Additional hexagonal WOFs are shown in *SI Appendix*, Fig. S2.

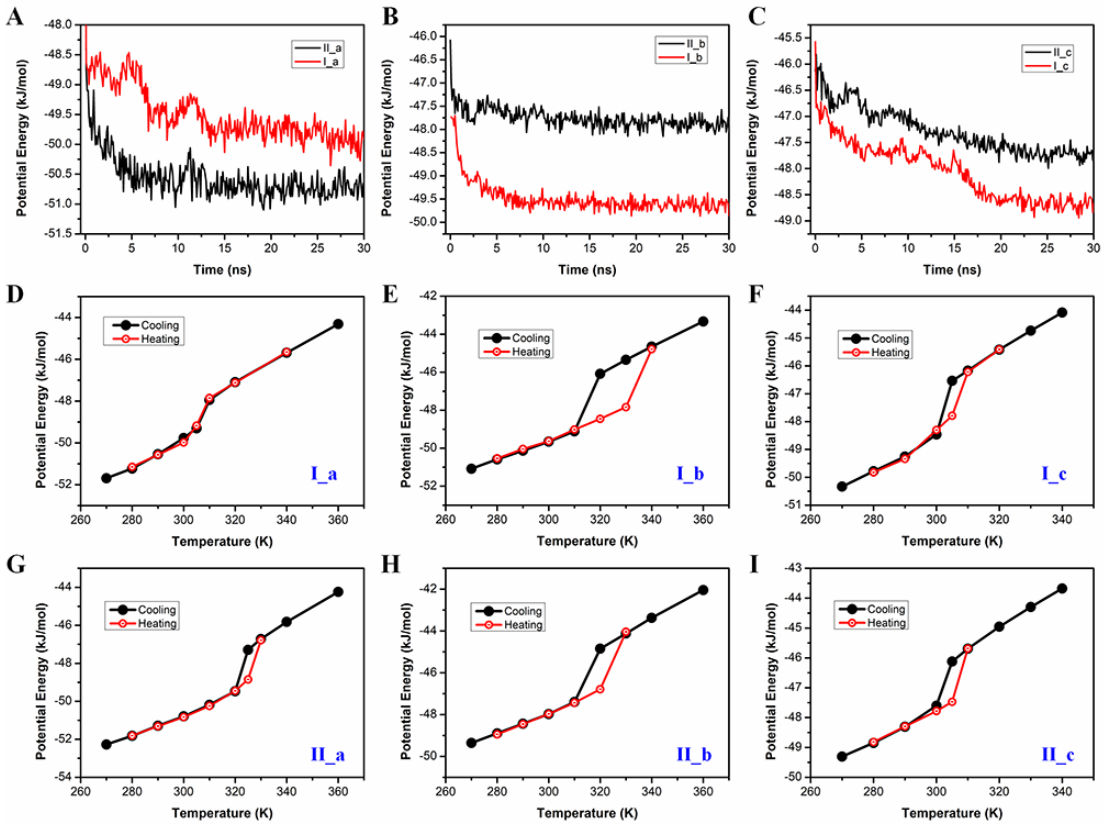

Fig. 2. Results of MD simulations to identify the freezing transitions from liquid water to the solid WOFs. (A)–(C) Potential energy versus simulation time during the phase transition processes in the MD simulations (see Fig. 1D for the corresponding six WOF structures) at a constant temperature of 300 K. (D)–(I) Potential energy versus temperature during the cooling and heating processes for each system.

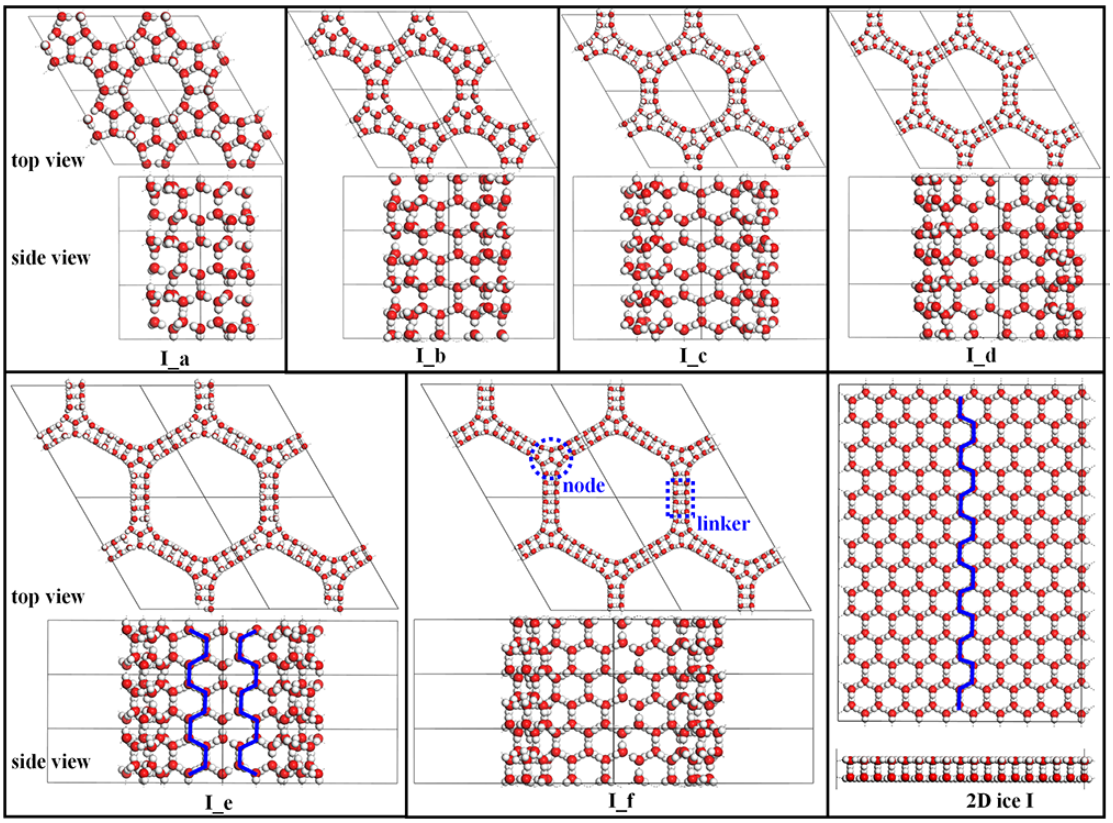

Fig. 3. Top and side views of the hexagonal unit cells of the six type-I WOFs. The nodes of the WOFs are composed of three edge-shared water pentagons, and the linkers are nanoribbons of hexagonal bilayer ice with varying width (see the panel for type-I_f WOF). The nodes and linkers are connected via the armchair edge of the AA-stacked hexagonal bilayer ice (as indicated by the blue line in the top view of 2D ice I). All the water molecules are coordinated with four neighboring water molecules, following the ice rules. The structures of the type-I WOFs are given in the Supporting files I_a.cif to I_f.cif.

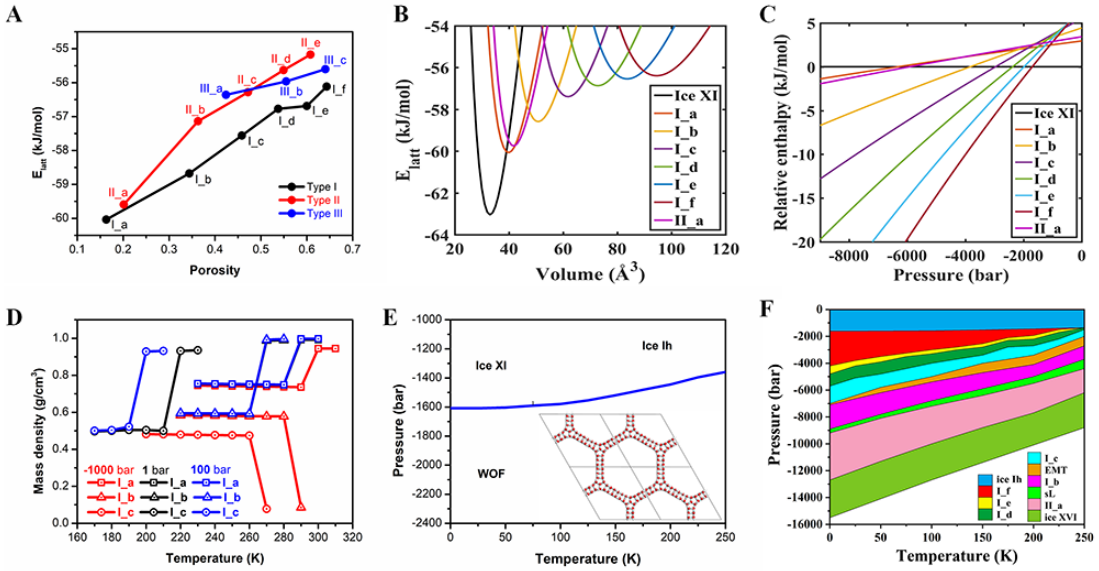

Fig. 4. Energies, thermal stabilities, and thermodynamic stabilities of the WOFs. (A) Lattice energy versus porosity for each WOF, computed based on the vdW-DF2 functional. (B) Lattice energy versus volume (per water molecule) for type-I and II_a WOFs, computed based on the vdW-DF2 functional. (C) Relative enthalpy of the WOFs versus negative pressure with respect to ice XI at 0 K, computed based on the vdW-DF2 functional. (D) Thermal stabilities of I_a, I_b, and I_c at −1000, 1, and 100 bar, examined via MD simulations with incremental increasing temperature (10 K), based on the TIP4P/Ice water model. (E) Pressure versus temperature phase diagram based on Gibbs free-energy computations. (F) Pressure versus temperature (*P*–*T*) phase diagram constructed on the basis of the computed Gibbs free energies and structural stabilities.

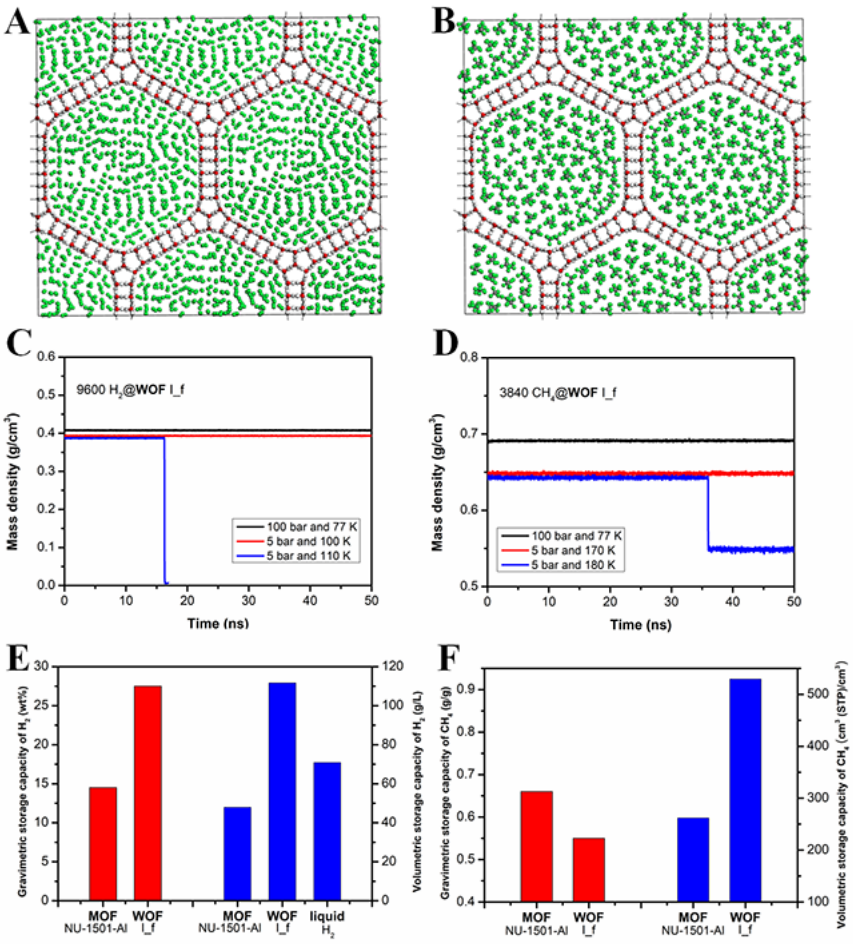

Fig. 5. Hydrogen and methane storage in a prototype WOF (I_f). (A) Initial structure of 9600 H_2 enclosed in the supercell of WOF I_f consisting of 2816 H_2O. (B) Initial structure of 3840 CH_4 enclosed in the supercell of WOF I_f consisting of 2816 H_2O. Color scheme: red spheres represent oxygen atoms of H_2O, white spheres represent hydrogen atoms of H_2O, green spheres represent hydrogen atoms of H_2 or CH_4, grey spheres represent carbon atoms of CH_4. (C) Thermal stability of WOF I_f as a hydrogen storage medium at 100 bar and 77 K, or at 5 bar and 100 – 110 K. (D) Thermal stability of WOF I_f as a methane storage at 100 bar and 77 K, or at 5 bar and 170 – 180 K. (E) Gravimetric storage capacity of H_2 (plotted in red) and volumetric storage capacity of H_2 (plotted in blue) in the MOF (structure taken from Ref. 32) and in WOF I_f at 100 bar and 77 K, respectively, as well as volumetric storage capacity of liquid H_2 at 1 bar and 20 K (taken from Ref. 33). (F) Gravimetric storage capacity and volumetric storage capacity of CH_4 in the MOF (structure taken from Ref. 32) and in WOF I_f at 100 bar and 77 K, respectively.